There may be differences between this version and the published version. You are advised to consult the published version if you wish to cite from it: https://doi.org/10.1016/j.jallcom.2022.168437

https://eprints.gla.ac.uk/289333/

Deposited on 13 February 2023

Influence of Zn and Ni dopants on the physicochemical and activity patterns of CoFe$_2$O$_4$ derived catalysts for hydrogen production by catalytic cracking of methane

Abdulrahman I. Alharthi [a]*, E. Abdel-Fattah [b], Justin S. J. Hargreaves [c], Mshari A. Alotaibi [a], Israf Ud Din [a], Matar N. Al-Shalwi[d]

[a] Department of Chemistry, College of Science and Humanities, Prince Sattam Bin Abdulaziz University, P.O. Box 173, Al-Kharj, 11942, Saudi Arabia.

[b] Department of Physics, College of Science and Humanities, Prince Sattam Bin Abdulaziz University, P.O. Box 173, Al-Kharj, 11942, Saudi Arabia.

[c] School of Chemistry, Joseph Black Building, University of Glasgow, Glasgow G12 8QQ, UK.

[d] Electrochemical Sciences Research Chair, (ESRC), Department of Chemistry, College of Science, King Saud University, P.O. Box 2455, Riyadh 11451, Saudi Arabia.

* Corresponding author, E-mail addresses: a.alharthi@psau.edu.sa

Abstract:

Zinc and nickel incorporated CoFe$_2$O$_4$ materials have been synthesized via a wet chemical method. Characterization of these cobalt ferrite based catalysts was undertaken using scanning electron microscopy (SEM), X-ray diffraction (XRD), X-ray photoelectron spectroscopy (XPS), Raman spectroscopy, and thermal gravimetric analysis (TGA). The catalytic activity of these materials was evaluated by monitoring the direct cracking of methane for the production of hydrogen and carbon. The XRD and SEM results indicated that Ni incorporation preserves the inverse spinel structure of CoFe$_2$O$_4$, whilst Zn incorporation changes its microstructure. The Co 2p, Fe 2p and O 1s XP spectra confirm the expected oxidation states of the elements in the near surface region of the catalysts. Raman spectra indicate cation redistribution between tetrahedral and octahedral sites upon Ni and Zn incorporation into CoFe$_2$O$_4$. BET surface area analysis revealed Ni incorporation is more effective in increasing the surface area of CoFe$_2$O$_4$ compared to Zn incorporation. Indeed, catalytic activity evaluation showed that Ni incorporation into CoFe$_2$O$_4$ improved methane conversion and correspondingly the hydrogen formation rate. In contrast, Zn incorporation led to very low catalytic activity.

The spent catalysts were further characterized and the results are strongly correlated with catalytic activity.

1. Introduction

Global warming is argued to be a serious threat to the natural environment [1-5]. Methane emissions have been observed mostly from oil, gas and agricultural related sources with other sources contributing. The Climate and Clean Air Coalition (CCAC), United Nations Environment Programme (UNEP) published the latest global methane assessment report in 2021 [6]. The report detailed the deleterious effect of methane upon human health. It was reported that methane emissions are contributing more severe damage to the environment than previously understood. It is stated that methane emission apparently causes thousands of deaths per annum due to air pollution and simultaneously leads to a rapid increase in average global temperature. Methane emissions can be mitigated in a number of ways, however catalytic cracking of methane to produce hydrogen offers not only a reduction in methane concentration but also clean fuel generation in the form of hydrogen.

The process of the direct cracking of methane results two valuable products, hydrogen and nano-structured carbon. The direct cracking of methane reaction can be described by equation (1):

$$CH_4 \quad \rightarrow \quad 2H_2 + C \quad \Delta H^\circ_{298K} = 75 \text{ kJ/mol} \qquad (1)$$

Hydrogen can be considered a promising clean fuel for use, for example, in fuel cell technologies. In addition, pure hydrogen can be used in many petrochemical processes. The second product of the methane cracking reaction, carbon, is also considered an added value material since it has distinctive physical properties, for example mechanical strength, high specific surface area and high resistance to strong acid and base solutions, making it potentially beneficial in many applications such as a H_2 storage material and as a catalyst support [7]. Many metals have been applied as catalysts for the catalytic cracking of methane. Pd, Pt, Fe, Co and Ni are considered as effective catalysts especially

when supported on metal oxides such as SiO_2, Al_2O_3, TiO_2 and MgO. Ni, Fe and Co have been widely investigated because of their lower price and relative abundance compared to noble metals. Regardless of the noble metals, the activity of Ni is the highest, followed by Co, and then Fe. In general, these transition metals have high activity for methane cracking reaction due to the presence of partially filled 3d orbitals facilitating the dissociation of the hydrocarbon molecules by interaction between the transition metal and hydrocarbon molecule. This interaction transferers the electrons by a back-donation process between the metal orbital and the orbitals of the hydrocarbon molecule and vice versa. Therefore, the electronic structure of the adsorbed molecule (CH_4) will change and thus, the molecule undergoes dissociation [8-12].

Methane is particularly stable amongst the hydrocarbons and is thermally stable up to 1030 °C [9] with temperatures around 1200 – 1300 °C being required to efficiently crack methane in the gas phase. However, the application of catalysts reduces the activation energy of this process by contributing reaction pathways of lower activation energy. Generally, catalytic methane cracking has been carried out in the temperature range of 500 to 900° C. High thermal stability is a prerequisite for a catalyst to be considered for methane cracking to produce hydrogen.

Cobalt ferrite ($CoFe_2O_4$) has been documented to possess high thermal stability even up to 1000 °C [13, 14]. The high thermal stability associated with $CoFe_2O_4$ enables it to be a potential candidate for methane cracking to produce hydrogen. $CoFe_2O_4$ is a well-known material with a variety of properties and applications like its magnetization, electrochemical properties, thermochemical properties, application in sensors, recording device applications, drug delivery applications, biomedical applications, and use in biotechnology [15]. In a previous study [16], the performance of pure $CoFe_2O_4$ and Cu and Mg doped $CoFe_2O_4$ for methane cracking at 800 °C was investigated. It was observed that the incorporation of Mg improved the performance of $CoFe_2O_4$ and improved the methane conversion up to 40 % and a maximum hydrogen formation rate of 13.2 x 10^{-6} mol H_2 g^{-1} s^{-1}, while the incorporation of Cu led to poor catalytic performance compared to pure $CoFe_2O_4$. To optimize $CoFe_2O_4$ for methane cracking, greater understanding of the role of doping metal as promoter is necessary. The appropriate choice of the promoter

type/quantity can improve catalyst performance and stability by enhancing the textural properties and controlling the oxidation state of the catalyst.

The current study partially addresses this requirement with an investigation of Zn^{2+} and Ni^{2+} doped $CoFe_2O_4$ synthesized using a wet chemical method. Nickle is known to have high catalytic efficacy for methane decomposition [17, 18] and Zinc metal, which is one of group 12 elements in the periodic table, has been used as promoter for the catalysts; for instance, in $Ni-Cu-Zn/Al_2O_3$ and $Zn-Ni/Al_2O_3$ catalysts for methane decomposition [19, 20], $Zn-Co/ZrO_2$ catalyst for dry reforming of methane [21] and M (Fe, Co, Ni, Cu, Zn)-Ce bimetal catalysts for steam reforming of hydrocarbon fuels [22]. Further, Zinc is a cheap metal, non-toxic and environmentally friendly in industrial application scale [23]. So far, to our knowledge, there were no reported studies on the effect of incorporation Zn^{2+} and Ni^{2+} promoters on the catalytic activity of $CoFe_2O_4$, which is attempted in this work. The effects of doped Zn^{2+} and Ni^{2+} ions have been thoroughly investigated by application of a range of techniques and in terms of performance for methane cracking using a fixed bed reactor. The physicochemical properties of the spent catalysts have been determined and the results correlated with catalytic performance.

2. Materials and experiments

2.1. Synthesis of metal ferrite materials

Loba Chemie Pvt. Ltd. provided analytical grade chemicals, which were used without any additional purification. A wet chemical method was used to make the parent cobalt ferrite material [24]. In a typical technique, 200 mL-distilled water was used to produce 0.1 M cobalt nitrate and 0.2 M ferric nitrate. The solution was heated to 85 °C. Aqueous ammonia was added dropwise to raise the pH of the solution to 10. The solution was stirred for two hours before being dried in an oven at 110 °C. Using nitrate salts of the relevant metals, the same approach was used to incorporate Zn^{2+} and Ni^{2+} ions in the parent $CoFe_2O_4$. Such incorporated $CoFe_2O_4$ catalysts were formulated as $Zn_{0.2}Co_{0.8}Fe_2O_4$ and $Ni_{0.2}Co_{0.8}Fe_2O_4$ catalysts. The dried materials were crushed into powder and calcined in air at 500 °C for 4 hours in a muffle furnace.

2.2. Characterization techniques

Different approaches were used to characterize fresh and spent materials. An X-ray diffractometer (Rigaku International) operating using Cu K_α radiation (of wavelength =1.5406 A) scanning over a 2θ range from 10° to 80° was applied for crystalline phase identification. The surface morphology of the catalysts was examined using a field-emission scanning electron microscope (FESEM) (QUANTA 250 FEI; USA). X-ray photoelectron spectroscopy (XPS) was used to investigate the near-surface chemical composition and oxidation states of materials. A Thermo K Alpha spectrometer with a spot size of 400 microns and charge correction employing Al K alpha X-rays (1486.6 eV) was employed. In addition, as an internal standard, all binding energy estimates were calibrated to C 1s = 284.5 eV. Raman spectra were collected with a Micro Raman (SENTERRA II, Brucker) spectrometer operating at a wavelength of 532 nm, a spectral resolution 5 cm^{-1}, and a laser spot size and power of 2μm and 6.5 mW, respectively. Thermogravimetric analyses were carried out in air with a temperature range of 25 to 1000 °C applying heating ramp rate of 10 °C/min. The TGA analysis was undertaken with a Netzsch proteus 70 instrument. The surface area and pore size of the catalysts were measured using N_2 physisorption isotherms determined at liquid nitrogen temperature using a Quantachrome Autosorb IQ model ASIQA3V600000-6 instrument.

2.3. Catalytic activity experiment

A 50 cm long fixed-bed quartz reactor tube with a 1.5 cm internal diameter was employed for the determination of the activity of cobalt ferrite materials. In the center of the reaction tube, 0.5 g of unreduced material was inserted and held in place with ceramic fiber plugs. The materials did not undergo reduction treatment prior to reaction. The current study used an AHG-supplied feed gas ratio of 25% nitrogen and 75% methane. The nitrogen component gas was employed as an internal standard to correct for the molar expansion which occurs upon reaction. A feed gas flow rate of 20 mL/min and a reaction temperature of 800 °C were used. On-line gas chromatography (using an Agilent GC Model 7890B equipped with 19043 Restek Micropacked GC Columns, Shin carbon

ST 80/100 2 M, 0.53 mm, and a thermal conductivity detector) was used to detect and quantify the gas-phase reaction products. Only nitrogen, methane, and hydrogen gases were detected.

3. Results and discussion

3.1. Characterization of the as prepared materials

3.1.1. SEM analysis of the fresh materials

Fig. 1 presents the SEM images of the as prepared $Zn-CoFe_2O_4$ and $Ni-CoFe_2O_4$ materials. The fresh $Zn-CoFe_2O_4$ material (Fig.1 (a)) has the form of solidified magma with tiny grooves, meanwhile, the $Ni-CoFe_2O_4$ material (Fig.1 (b)) resembles bulky-microstructures fractured into small chunks with tiny pores and grooves. It can be seen that, the type of incorporating ion affects the morphology and microstructure of the sponge-like shape $CoFe_2O_4$ material, which was reported in a previous study [16]. The presence of the porous–tiny groves structure is potentially advantageous in catalytic application as it can offer a large amount of accessible active sites and enhance reactant diffusion [25].
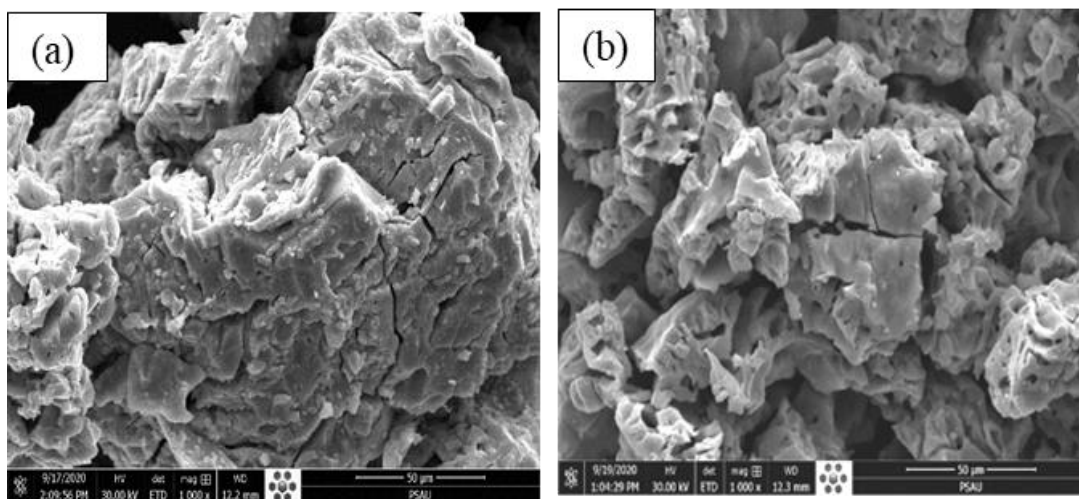
Fig. 1. SEM images of as prepared (a) $Zn-CoFe_2O_4$ and (b) $Ni-CoFe_2O_4$, materials.

3.1.2. Measurement of textural properties

Fig. 2 displays the N_2 adsorption-desorption isotherms of the fresh $Zn-CoFe_2O_4$ and $Ni-CoFe_2O_4$ materials measured at 77 K. The hysteresis loop of $Ni-CoFe_2O_4$ material covers a wide range of $p/p^o \sim 0.52 - 0.95$ in comparison to $p/p^o \sim 0.58$ to 0.95 of $Zn-CoFe_2O_4$ material, implying that the $Ni-CoFe_2O_4$ material contains wide range of mesoporous size pores. The resulting hysteresis loop in these samples could be ascribed to factors such as pore shape, weak adsorbate-absorbent interaction potentials [26, 27]. Further, the capillary condensation occurs at relative high pressures, confirms that the mesopores in the samples were irregular.
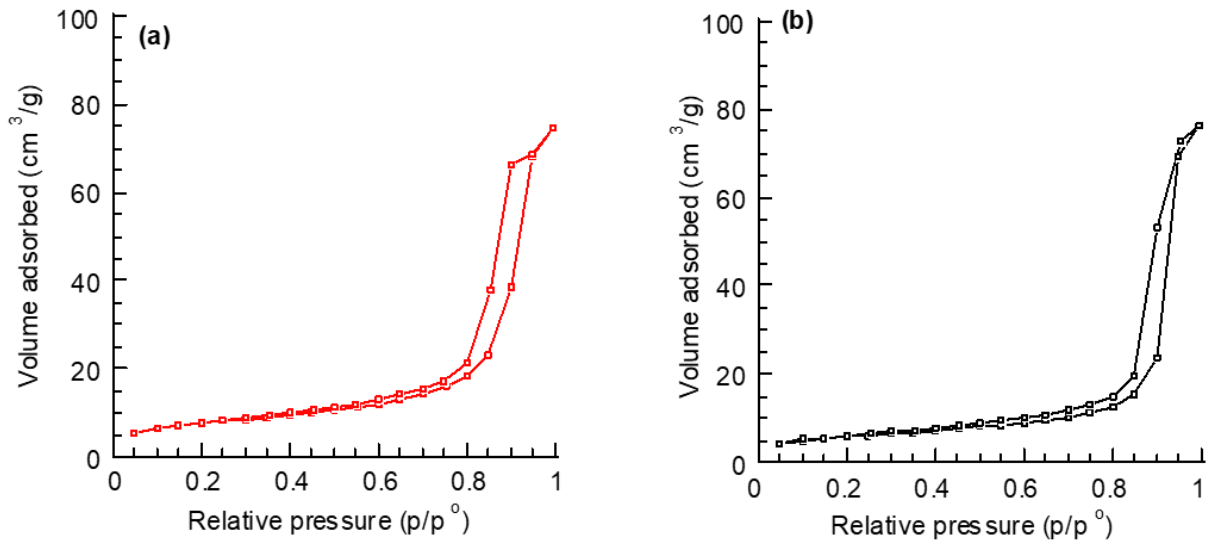
Fig. 2. N_2 adsorption isotherms of the fresh (a) $Zn-CoFe_2O_4$ and (b) $Ni-CoFe_2O_4$ materials.

Table 1 presents the BET surface areas of fresh $Zn-CoFe_2O_4$ and $Ni-CoFe_2O_4$. The addition of Zn^{2+} into the fresh $CoFe_2O_4$ catalyst did not significantly affect its surface area [16]. For the fresh $Ni-CoFe_2O_4$ catalyst, it seems that the addition of Ni^{2+} enhanced the surface area of $CoFe_2O_4$, which increased from 25 to 45 m^2/g. This is consistent with the smaller size of the fresh $Ni-CoFe_2O_4$ particles in comparison to those for $Zn-CoFe_2O_4$, as can be seen in the SEM images in Fig.1.

Table 1 Textural properties of the materials. Specific surface area, pore volume and pore radius.

Catalyst	Surface Area (m²/g)	Pore Volume (cc/g)	Pore Radius (A⁰)	Ref.
$CoFe_2O_4$	25	0.12	88	[16]
$Zn-CoFe_2O_4$	26	0.12	17	
$Ni-CoFe_2O_4$	45	0.14	61	

3.1.3. XRD patterns

Fig. 3 (A) presents the X-ray diffraction patterns of the fresh $Zn-CoFe_2O_4$ and $Ni-CoFe_2O_4$ materials. The XRD pattern of $CoFe_2O_4$ is plotted for comparison [16]. As evident, $Zn-CoFe_2O_4$ and $Ni-CoFe_2O_4$ materials displayed reflections that coincide with that of $CoFe_2O_4$, implying the presence of $CoFe_2O_4$ related phases. For instance, one can observe the (111), (220), (311), (400), (422), (511), (440) and (533) reflections, at 18.36^o; 30.19^o; 35.54^o; 43.19^o; 53.62^o; 57.1^o; 62.67^o and 74.12^o 2Θ respectively. No reflections corresponding to segregated Zn and Ni containing phases were observed, which is consistent with high dispersion of Zn^{2+} and Ni^{2+}.
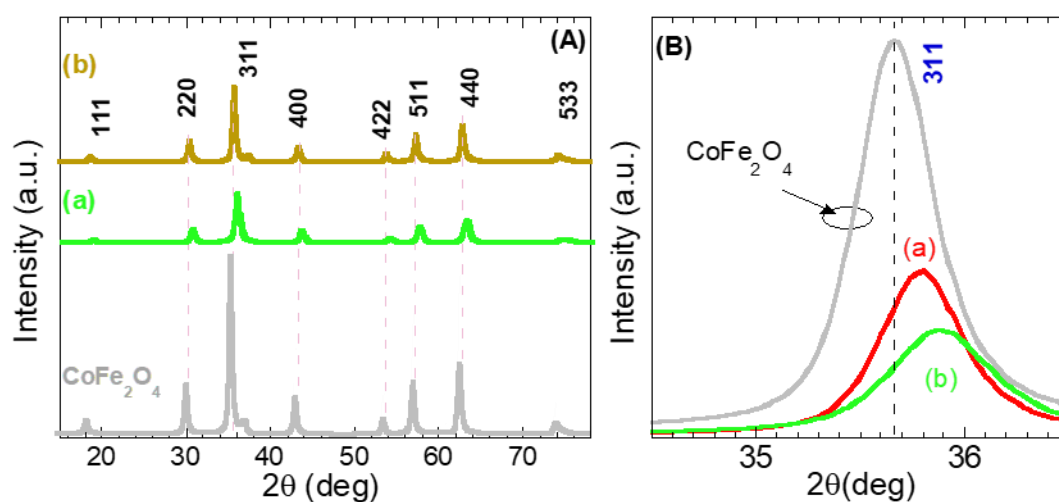
**Fig. 3. (a)** XRD patterns of fresh materials and **(b)** Zoomed view of the (311) reflection for (a) $Zn-CoFe_2O_4$ and (b) $Ni-CoFe_2O_4$.

The XRD patterns indicate that the inclusion of Zn^{2+} and Ni^{2+} dopants doesn't alter the $CoFe_2O_4$ spinel phase [16], although the intensity of the reflections is remarkably decreased in comparison to undoped $CoFe_2O_4$. The decrease in peak intensity of $CoFe_2O_4$ indicates loss of crystallinity. Fig. 3 (B) shows an expanded view of the most intense peak (the (311) reflection), it is clear that the peak position is shifted to larger 2θ angles upon Zn^{2+} and Ni^{2+} addition. The change of the peak position can be attributed to the incorporation of the dopants into the lattice. The Co^{2+}, Zn^{2+} and Ni^{2+} ionic radii are 0.745, 0.74 and 0.69 Å, respectively [28]. Therefore, the replacement of Co^{2+} ions with Zn^{2+} and Ni^{2+} ions would affect the lattice parameter of $CoFe_2O_4$. The lattice parameter "a" and crystallite size for the samples were calculated using the (311) reflection, and are summarized in Table 2. The calculated lattice parameters, "a", are 8.325 and 8.307 Å for Zn-$CoFe_2O_4$ and Ni-$CoFe_2O_4$, respectively. The reduced lattice parameter "a" of $CoFe_2O_4$ upon Zn^{2+} and Ni^{2+} incorporated, potentially suggests variation in the catalyst microstructure, as well as redistribution of cations among octahedral and tetrahedral sites in cubic spinel structure [29] in conjunction with the Raman spectra discussed below. Fig. 3(B) shows also, that the (311) peak broadening increases in Zn-$CoFe_2O_4$ and Ni-$CoFe_2O_4$ in comparison to that in $CoFe_2O_4$, suggesting – if broadening can be solely attributed to coherent diffraction domain size - that the crystallite size of $CoFe_2O_4 > Zn$-$CoFe_2O_4 > Ni$-$CoFe_2O_4$.

Table 2 The calculated crystal size and lattice parameters of the examined materials.

Sample	Crystal size (nm)	d spacing (Å)	a (Å)	Ref.
$CoFe_2O_4$	19.7	2.52	8.357	[13]
Zn-$CoFe_2O_4$	18.4	2.51	8.33	
Ni-$CoFe_2O_4$	17.8	2.50	8.307	

3.1.4. Raman spectroscopy

Raman features of ferrites in cubic structures are highly specific, i.e. they depend on cation distribution, stoichiometry, defects, as well as the experimental conditions. Group theory analysis predicts 5 Raman modes namely $^1T_{2g}$, E_g, $^2T_{2g}$, $^3T_{2g}$ and A_{1g} to be exist in ferrites possessing the spinel (Fd3m) structure. However, additional modes (up to 10 modes) might appear in the vibrational spectra due to local distortions of the ferrite lattice [18].
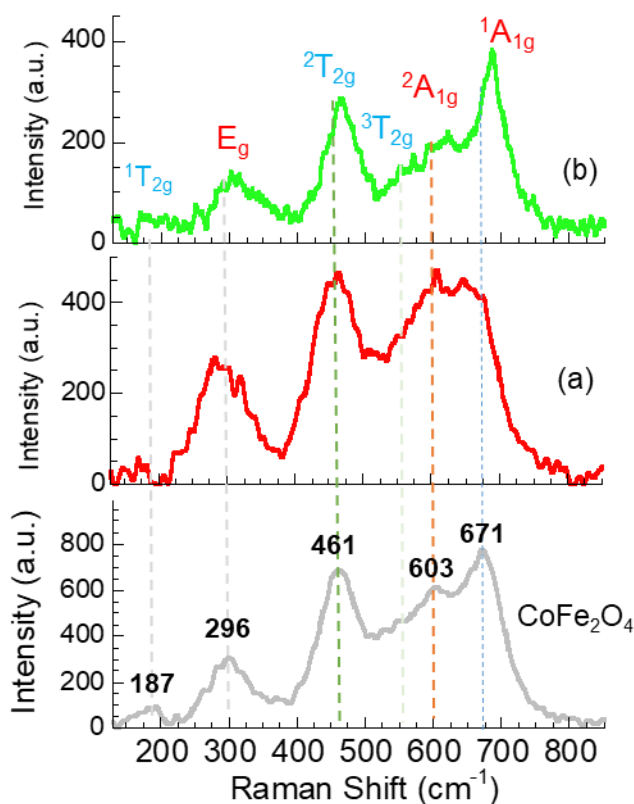
Fig.4. Raman spectra of fresh (a) Zn-CoFe$_2$O$_4$ and (b) Ni-CoFe$_2$O$_4$ materials.
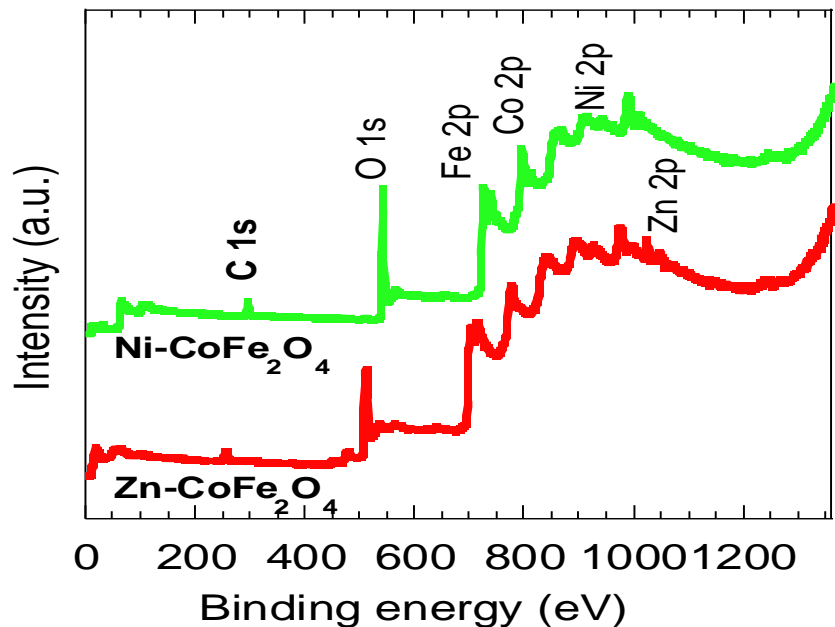
The Raman spectra of Zn-CoFe$_2$O$_4$ and Ni-CoFe$_2$O$_4$ correspond to CoFe$_2$O$_4$, [16] as they possess 6 vibration modes, which are characteristic of ferrites with a spinel (Fd3m) structure: $^1A_{1g}$, $^2A_{1g}$, $^3T_{2g}$, $^2T_{2g}$, E_g and $^1T_{2g}$ at 671 cm^{-1}, 603 cm^{-1}, 545 cm^{-1}, 461 cm^{-1}, 296 cm^{-1} and 187 cm^{-1}, respectively [30,31]. The A_{1g} mode represents symmetric stretching of Fe^{3+} and O^{2-} ions in a tetrahedral site (A site), whilst the low frequency modes E_g and T_{2g} are due to the symmetric and antisymmetric bending of oxygen species

in M-O bonds at octahedral sites (B sites) [32,33], where M refers to either Co^{2+} and Fe^{3+} ions. The presence of the $^2A_{1g}$ mode is a typical feature of inverse-mixed spinel's [34]. The A_{1g} mode contains a mixture of Co^{2+}, Fe^{3+} ions; $^1A_{1g}$ corresponds to Fe^{3+} and $^2A_{1g}$ assigned to the Co^{2+} cations located at the tetrahedral site. Hence, the $^2A_{1g}$ / $^1A_{1g}$ ratio indicates the Co^{2+}/Fe^{3+} tetrahedral site ratio. Furthermore, since the A_{1g} and $^2T_{2g}$ modes occur due to vibration of oxygen associated with tetrahedral and octahedral cation sites, respectively, then the ratio $^2T_{2g}/^1A_{1g}$ indicates the cation distributions in octahedral to tetrahedral sites [34]. From Fig.4 (a, b), it can be seen that the peak intensity, positions and shape are slightly changed in comparison with those of $CoFe_2O_4$, suggesting a redistribution of cations in the spinel lattice. As known, there is a strong correlation of the frequencies of the modes with the ionic radius/mass of the incorporated ions. For example, the A_{1g} mode in the Raman spectrum of $Zn-CoFe_2O_4$ is getting broadening over Zn^{2+} incorporating in $CoFe_2O_4$. Moreover, the $^2T_{2g}$ peak intensity of $Zn-CoFe_2O_4$ increases in comparison to that of $CoFe_2O_4$. The $^2T_{2g}/^1A_{1g}$, ratio for $Zn-CoFe_2O_4$ is 1.03, which is greater than the 0.888 for the $CoFe_2O_4$ parent [16]. Higher $^2T_{2g}/^1A_{1g}$ ratios indicate a reduction in the inversion degree [35, 36] i.e. confirming cation redistribution and that more Zn^{2+} ions preferably migrate to the tetrahedral sites. Incorporating Zn^{2+} forces Fe^{3+} cations to migrate from tetrahedral sites to occupy octahedral sites resulting in increasing $^2T_{2g}$ peak intensity and thereby, reducing the inverse spinel system structure. The presence of different cations (Zn^{2+}, Co^{2+}, and Fe^{3+}) which vibrate at different characteristic frequencies gives rise to broad-shouldered peaks as seen for A_{1g} mode in Fig. 4 (b).

On the other hand, the $^1A_{1g}$ and $^2A_{1g}$ modes in $Ni-CoFe_2O_4$ are shifted to the higher wavenumbers (blue shift); owing to the slightly lower atomic mass of Ni^{2+} (58.69) as compared to Co^{2+} (58.933) [28]. Furthermore, the symmetry of the $^1A_{1g}$ mode in Fig. (c) suggests that Ni^{2+} (0.69 Å) ions replaced Co^{2+} (0.58 Å) ions in tetrahedral sites, hence changing the energy of their bending. The calculated $^2T_{2g}/^1A_{1g}$ ratio for $Ni-CoFe_2O_4$ is 0.742, while it was 0.888 for $CoFe_2O_4$ [16], i.e. Ni^{2+} incorporation into $CoFe_2O_4$ led to cation redistribution.

3.1.5. X-Ray photoelectron spectroscopy (XPS)

Fig.5 shows the XPS survey spectra of the fresh Zn^{2+} and Ni^{2+} incorporated $CoFe_2O_4$. The measurements were performed in flooding mode in the binding energy (BE) range of 10 to 1360 eV. The examined spectra show sharp peaks of BE at ca. 530.9, 710 and 779.9 eV assigned to oxygen (O1s), iron (Fe 2p) and cobalt (Co 2p), respectively, characteristic of $CoFe_2O_4$. Additional peaks at ca. 1051 eV and 856.5 eV can be assigned to zinc (Zn 2p) and nickel (Ni 2p), respectively for the doped materials. The broad peaks in the 830– 930 eV region in all samples are assigned to the Fe LMM Auger transitions [37]. In addition, a very small peak can be observed at ca. 285 eV corresponding to carbon (C 1s) in all samples. The near surface elemental analysis is summarized in Table 3. The XPS results confirm the chemical compositions of the examined catalysts. As one can see, the percentage of Fe 2p and Co 2p are varied upon the incorporation of Zn^{2+} and Ni^{2+} ions with respect to pure $CoFe_2O_4$ [16]. This is an indication of the cation redistribution occurs upon Zn^{2+} and Ni^{2+} incorporated $CoFe_2O_4$ catalyst. This observation agrees well with Raman results and predicts the variation of the examined catalyst performance.

**Fig.5.** XPS survey spectra of fresh $Zn-CoFe_2O_4$ and $Ni-CoFe_2O_4$ materials.

Table 3 The elemental analysis of the examined materials from XPS survey spectra.

Catalyst	Fe 2p %	Co 2p %	O 1s %	C 1s %	Ni 2p %	Zn 2p %	Ref.
$CoFe_2O_4$	19	14	51	15	-----	-----	[13]
$Zn-CoFe_2O_4$	23	9	49	16	-----	2	
$Ni-CoFe_2O_4$	19	11	52	16	1	-----	

To identify the various near surface cations in the examined catalysts, high-resolution Co 2p, Fe 2p and O 1s XP spectra were measured and are shown in Fig.6 (a-f). The Co 2p spectrum of $Zn-CoFe_2O_4$ exhibits two doublets - Co $2p_{3/2}$ and Co $2p_{1/2}$ - and satellites at higher BE side of Co $2p_{3/2}$ and Co $2p_{1/2}$ as seen in Fig.6 (a). The Co $2p_{3/2}$ peak can be resolved into three sup-peaks; 779.50 eV corresponds to Co bonded to oxygen species (Co-O) or Co^{2+} in octahedral sites, 781.8 eV can be assigned the Co^{2+} in the tetrahedral site and 783.8 eV represents $Co^{2+}-OH$ on the catalyst surface [39]. Similarly, the Co 2p ½ peak can be de-convolved into peaks at 794.4 eV and 796.6 eV. The satellite peaks (Co 2p_sat.) at binding energies of 785 and 805 eV demonstrates the presence of cobalt in oxide form. The Co 2p peaks of $Ni-CoFe_2O_4$ (Fig. 6 (d)) have an absence of sub-peak at 783.8 eV that represents $Co^{2+}-OH$, suggesting less near surface oxygen/hydroxyl. The high-resolution Fe 2p spectrum from $Zn-CoFe_2O_4$ shown in Fig. 6 (b) reveals two doublets characteristic of Fe $2p_{3/2}$ and Fe $2p_{1/2}$ and satellites at higher energies [38]. The Fe $2p_{3/2}$ peak can be fitted by three sup-peaks; at 710.0 eV corresponding to Fe^{3+} cations located at octahedral (B) sites, at 712.6 eV attributed to tetrahedral (A) sites, and a peak at *ca.* 714 eV probably assigned to Fe^{3+} bound to OH or COO species on the catalyst surface [39]. The Fe $2p_{1/2}$ spectrum from $Zn-CoFe_2O_4$ can be decomposed into two peaks at 723 eV and at 726.2 eV corresponding to Fe^{3+} in B and A sites, respectively. Again, the Fe2p spectra of $Ni-CoFe_2O_4$ (Fig.6 (e)) shows the absence of the peak at 714 eV ($Fe^{+3}-OH$) related to adsorbed OH on the catalyst surface. The O 1s spectrum shown in Fig. 6 (c, f), is comprised of 3 peaks; a peak at 529.2 eV ($O_{latt.}$) attributed to lattice oxygen (Co−O and Fe−O), a peak at 530.8 eV associated with oxygen vacancies and a peak at 532.1 eV ($O_{adsorbates}$) attributed to adsorbed H_2O on the surface of $CoFe_2O_4$ catalyst [28]. The Co 2p, Fe 2p and O 1s for Zn^{2+} and Ni^{2+} incorporated $CoFe_2O_4$ peaks

are different in shape and intensity, compared to fresh $CoFe_2O_4$ [16], suggesting redistribution of the cations between the A and B sites. Furthermore, the oxygen vacancy component ($O_{vacancy}$) of the O 1s spectrum of $Ni-CoFe_2O_4$ (Fig.6 (f)) is relatively increased in comparison to that of $Zn-CoFe_2O_4$. The increase of oxygen vacancy component improves the conductivity and implies enhancement of surface redox reaction processes.
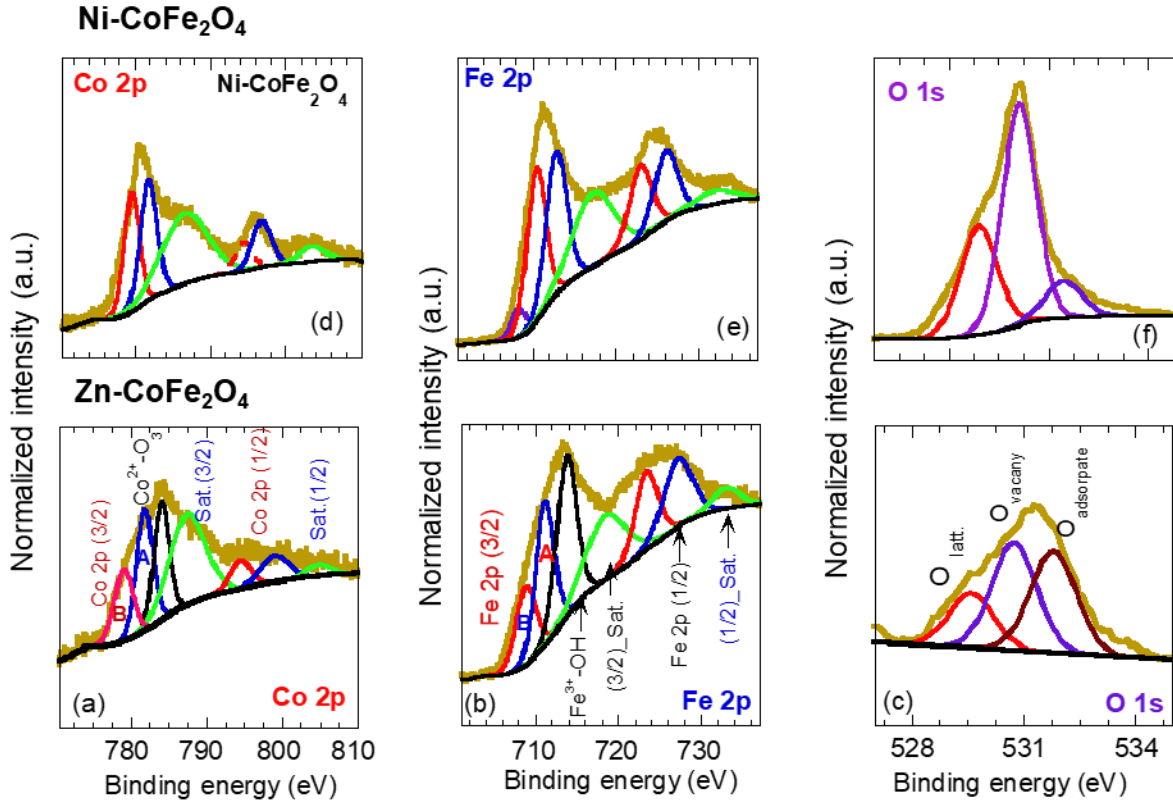

Fig. 6. High resolution spectra of Co 2p, Fe 2p and O 1s for fresh (a, b, c) Zn- $CoFe_2O_4$ and (d, e, f) $Ni-CoFe_2O_4$.

4. Catalyst activity studies

The catalytic activity of $Zn-CoFe_2O_4$ and $Ni-CoFe_2O_4$ c for direct cracking of methane was investigated in terms of percentage of methane conversion and hydrogen formation rate as a function of time on stream (TOS) as shown in Fig. 7 (a, b). Surprisingly, the $Zn-CoFe_2O_4$ catalyst showed very poor activity compared to other catalysts. The maximum methane conversion and hydrogen formation rate were ~3 %   and 0.11 x 10^{-6} mol H_2 g^{-1}

s^{-1}, respectively. In contrast, the catalytic activity of Ni-CoFe$_2$O$_4$ was very significant, where the maximum methane conversion was ~50 % and hydrogen formation rate of 16.8 x 10^{-6} mol H$_2$ g^{-1} s^{-1}. This result is higher than that previously observed [16] for CoFe$_2$O$_4$ and Mg-CoFe$_2$O$_4$ derived catalysts, under comparable reaction conditions, as they exhibited methane conversion of 31.6% and 40.0 %, respectively. In addition, it was noted that the incorporation of Ni^{2+} in CoFe$_2$O$_4$ reduced the induction period from 180 to 150 min. Further, the methane cracking profile of Ni-CoFe$_2$O$_4$ is different from that of Ni-Co/AC and Ni-Fe/AC catalysts [40], as methane conversion decreased from 80% to 15% within about 100 min at a reaction temperature of 850 °C. Moreover, the methane conversion achieved for Ni/Al$_2$O$_3$, Ni-Co/Al$_2$O$_3$, Ni-Cu/Al$_2$O$_3$ and Ni-Fe/Al$_2$O$_3$ catalysts at 650 °C did not exceed 40% at the beginning of the reaction and decreased sharply after 40 min of time on stream [41]. This is probably due to the physiochemical properties of Ni-CoFe$_2$O$_4$ catalyst as well as to the reaction conditions that were applied. In contrast, deactivation of the Ni-CoFe$_2$O$_4$ derived catalyst was not observed during the testing period that lasted for 300 minutes. The shown hydrogen production value is the total hydrogen production over the whole reaction time. Hence, the total amount of hydrogen produced is *ca.* 600000 x 10^{-6} mol H$_2$ g^{-1} for Ni-CoFe$_2$O$_4$, which is higher than ca. 400000 x 10^{-6} mol H$_2$ g^{-1} s^{-1} for CoFe$_2$O$_4$ [16]. Methane decomposition experiments were conducted twice, and results are averaged.
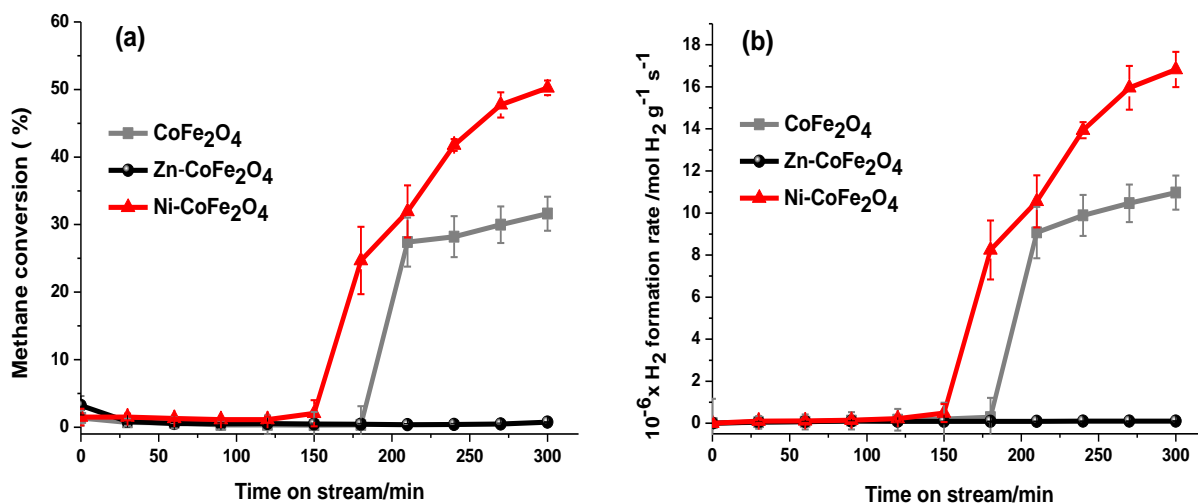
Fig. 7. (a) Methane conversion (%) and (b) hydrogen formation rate with time on stream (min) over Zn-CoFe$_2$O$_4$ and Ni-CoFe$_2$O$_4$, at 800 °C, 0.5 g material and 20 mL/min reactant gas flowrate.

It was reported that the size, composition, shape and surface features of catalysts are key factors affecting catalytic activity for catalytic decomposition of methane [42]. The low activity of Zn-CoFe$_2$O$_4$ is probably due to its physicochemical properties. For instance, the Raman results of Zn-CoFe$_2$O$_4$ sample confirm cation redistribution and the change of the original nature of CoFe$_2$O$_4$, possessing the inverse spinel system structure towards the normal spinel structure. From the XPS results, more iron Fe and less Co are present in the near surface region of the Zn-CoFe$_2$O$_4$ material compared to the other materials. Moreover, the O 1s XPS spectrum shown in Fig.6 (c), comprises a high-peak intensity of O$_{adsorbates}$ indicative of a large amount of adsorbed oxygen. In addition, SEM imaging of Zn-CoFe$_2$O$_4$ (Fig. 1 (a)) showed that its morphology looks similar to sintered magma corresponding to low dispersion.

Some previous studies have shown that Zn metal is inactive for methane decomposition, for example, Urdiana *et al* [43] studied the catalytic decomposition of methane over different transition metal such as Ni, Cu, Co, Mn, Fe, Zn, and W supported on SBA-15 as catalysts to produce hydrogen and carbon nanomaterials. They found that the Zn/SBA-15 catalyst showed poor conversion of methane. Ogihara and co-workers [44], investigated the catalytic activity of Pd/Al$_2$O$_3$ and Pd-M/Al$_2$O$_3$ catalysts (where M = Fe, Co, Ni, Cu, Zn, Ga, In, Sn, Au, Pb and Bi) for methane decomposition. They reported that Pd-Zn/Al$_2$O$_3$ hardly decomposed methane. In contrast, Ni-CoFe$_2$O$_4$ showed the highest activity compared to other materials. Nickel is an active metal for catalytic decomposition of methane in its different forms such as a monometallic catalyst, a bimetallic catalyst, and a component of mixed metallic catalysts [41]. Hence, it is clear that the addition of Ni^{2+} into CoFe$_2$O$_4$ improved catalytic performance. In addition, the BET surface area analysis showed Ni-CoFe$_2$O$_4$ to have a reasonably large surface area, which could play a role in enhancement of catalytic activity. The O 1s XS spectrum shown in Fig.6 (f), exhibited a low-intensity O$_{adsorbates}$ feature. Also, the Co 2p and Fe 2p XP spectra (Fig. 6 (d, e)) showed the absence of sub-peaks at 783.8 eV and 714 eV which correspond to Co^{2+}-OH and Fe^{+3}-OH, respectively. This suggests that the Ni-CoFe$_2$O$_4$ catalyst has less oxygen/hydroxyl component, which can facilitate the reduction process of Ni-CoFe$_2$O$_4$ i.e. leading to more rapid development and high catalyst activity.

# 5. Spent catalyst characterization

5.1. SEM analyses of spent catalysts

Fig. 8 shows the SEM images of the spent $Zn-CoFe_2O_4$ and $Ni-CoFe_2O_4$ derived catalysts. It could be seen that the $Zn-CoFe_2O_4$ derived material (Fig.8 a) is less dispersed and the original agglomerate morphology is preserved, which can be related to its low catalytic activity. In contrast, the SEM of spent $Ni-CoFe_2O_4$ derived catalyst shows a uniform spherical-like shape, high dispersion and small particle size, suggesting a higher external surface area. Interestingly, the spent $Ni-CoFe_2O_4$ material is covered with filamentous carbon structures as a by-product of the methane cracking process, whilst the spent $Zn-CoFe_2O_4$ material was without carbon deposited over the surface. The SEM images of spent catalysts are consistent with the catalytic performance shown in Fig. 7. Hydrocarbon cracking over metal particles results in carbon dissolution in the metal and then outward diffusion forming a filament with/without a naked metal particle at its tip [45]. This mechanism plays a role in keeping the catalyst active for long periods. Therefore, it suggests that the formation of filamentous carbon over the $Ni-CoFe_2O_4$ derived catalyst did not block the active sites on the catalyst surface, and hence it did not undergo deactivation during the time on stream, as seen in Fig. 7.
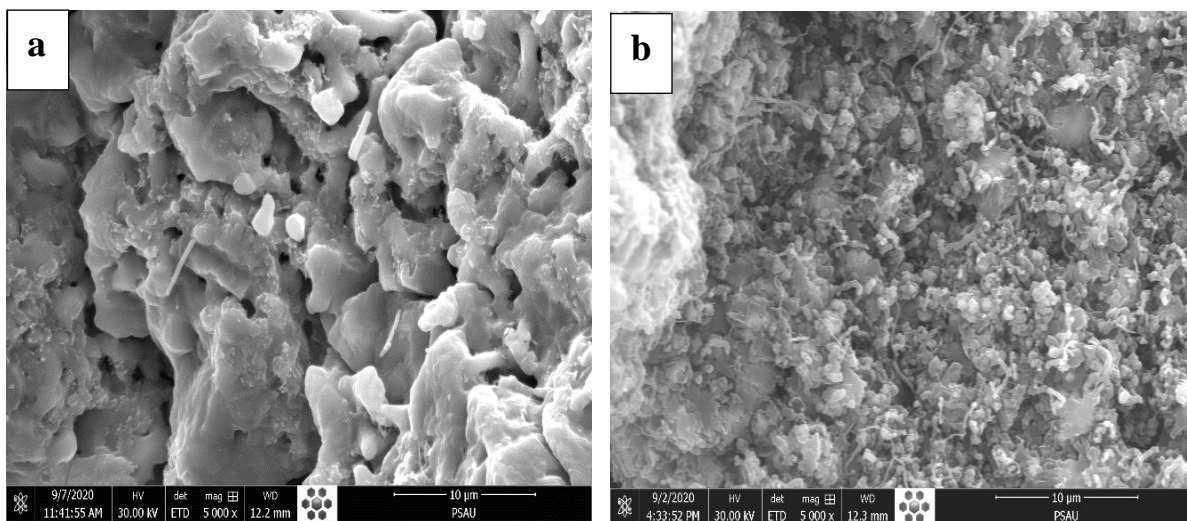
Fig. 8. SEM images of spent (a) $Zn-CoFe_2O_4$, (b) $Ni-CoFe_2O_4$ catalysts.

5.2   XRD studies

The spent catalysts obtained after methane cracking were further characterized by XRD and results are displayed in Fig. 9. It clear that, the spent catalyst lost their original spinel structure, irrespective of the catalyst component. The prevailing peaks in all spent catalysts are (110) and (200) reflections of α-Fe at 2θ 44.8° and 65.8° respectively. A peak at 2θ = 26.6°, assigned to the graphite (003) reflection, can be seen in the XRD pattern of the spent Ni-CoFe$_2$O$_4$ catalyst, while it was absent in that of spent Zn-CoFe$_2$O$_4$ catalyst. The observation of the graphite in the Ni-CoFe$_2$O$_4$ spent catalyst agree well with its SEM image (Fig. 8 (b)), and corresponds to the cracking of methane and carbon formation. Meanwhile its absence in the XRD pattern of the spent Zn-CoFe$_2$O$_4$ material is consistent with its deficient activity. Fig. 9 indicates that the spent Ni-CoFe$_2$O$_4$ catalyst is completely reduced, corresponding its high catalytic activity and in contrast the XRD pattern of the spent Zn-CoFe$_2$O$_4$ catalyst was not completely reduced as the cobalt remained in its oxidized state as also can be seen in Fig. 9. Incomplete reduction potentially a further reason that explains the very low catalytic activity of the Zn-CoFe$_2$O$_4$ catalyst.
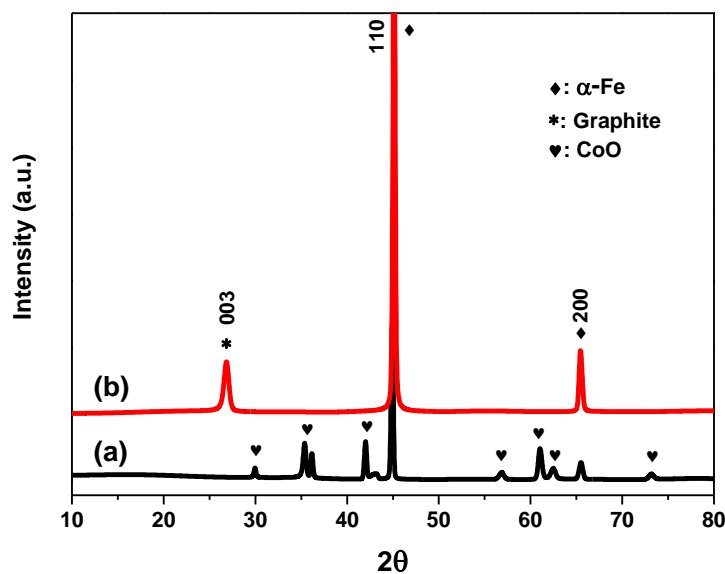
Fig. 9. XRD patterns of spent (a) Zn-CoFe$_2$O$_4$ and (b) Ni-CoFe$_2$O$_4$ catalysts.

5.3 Raman spectroscopy

Fig. 10. shows the Raman spectra of the spent catalysts. The Raman spectrum of the spent Zn-CoFe$_2$O$_4$ catalyst, Fig. 10 (a), contains a very weak D band at 1326 cm^{-1}, and some bands assigned to zinc and cobalt oxides, which is consistent with the XRD result (Fig.9 (a)).   Meanwhile, the Raman spectrum of the spent Ni-CoFe$_2$O$_4$ catalyst comprises sharp Raman bands at 1340, 1578 and 2542 cm^{-1}, corresponding to *D, G* and *2D* graphite bands, respectively [28]. Fig.10 (b) confirms the effectiveness of Ni-CoFe$_2$O$_4$ as a redox catalyst for methane cracking and is consistent with XRD and SEM results in terms of carbon formation. The *D* band represents the sp^3 disordered carbon mode, while the *G* band represent well-ordered sp^2 carbon mode. The intensity ratio of the D band and G band (I$_D$/I$_G$) is generally utilized for characterizing the defect volume in the structure of graphitic materials [46]. A higher I$_D$/I$_G$ ratio means that there is a large defect in the graphitic structure. Alternatively, a higher I$_D$/I$_G$ ratio means that more sp^2 bonds are broken and converted to sp^3 nanostructures. The I$_D$/I$_G$ ratio for spent Ni-CoFe$_2$O$_4$ catalyst is 0.26, which is smaller than that for pure CoFe$_2$O$_4$ catalyst [16] suggesting that the carbon deposited on spent Ni-CoFe$_2$O$_4$ material is less defects than that deposited on spent CoFe$_2$O$_4$.
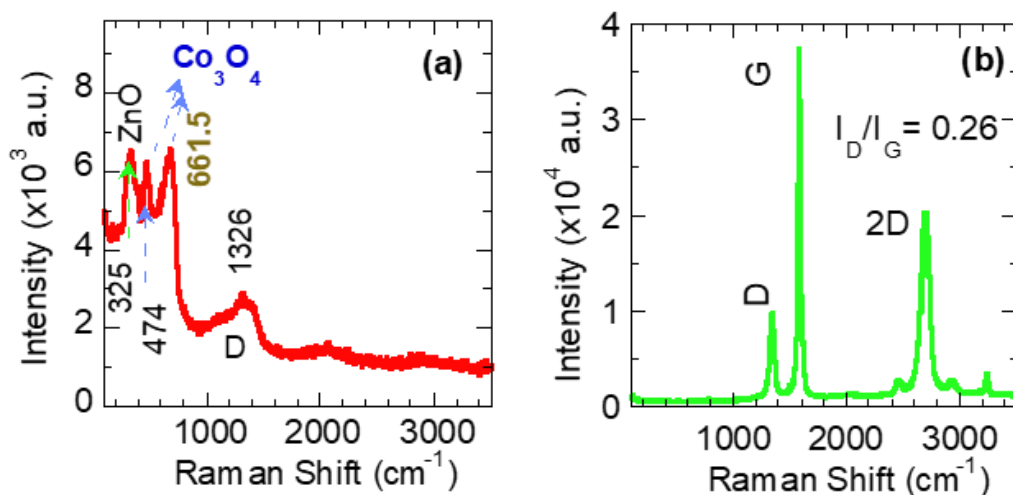
Fig. 10. Raman Spectra of spent (a) Zn- CoFe$_2$O$_4$ and (b) Ni- CoFe$_2$O$_4$ catalysts.

5.4. TGA studies

Fig. 11 (a, b) shows the TGA and DTG analyses of the spent $Zn-CoFe_2O_4$ and $Ni-CoFe_2O_4$ catalysts undertaken in air environment. Irrespective of the catalyst type, the TGA profile revealed a slight increase in weight until ~ 550 ^{o}C, beyond which the catalysts behave differently. The TGA of spent $Zn-CoFe_2O_4$ catalyst shows a rapid weight increase in the range 550-1000 ^{o}C, meanwhile, the TGA of spent $Ni-CoFe_2O_4$ undergo sudden drop in weight in the temperature range 550-680 ^{o}C, beyond which the residual catalysts weight was constant in the temperature range 680-1000 ^{o}C. The initial increase of catalysts weight attributed to the oxidation of the spent catalyst metals in air. The weight loss in the temperature range 550-680 °C resulted from the combustion of deposited carbon. The deposited carbon amount over $Ni-CoFe_2O_4$ catalyst is 37.35 wt%, which is larger than that (22.1 wt %) deposited over spent $CoFe_2O_4$ run under comparable conditions [16]. This is not surprising as $Ni-CoFe_2O_4$ showed higher methane conversion compared to $CoFe_2O_4$. For the spent $Zn-CoFe_2O_4$ catalyst, the increases of weight beyond temperature 550 ^{o}C suggested that carbon was not deposited on the $Zn-CoFe_2O_4$ catalyst during the methane cracking process. Rather the spent Zn-CoFe phases undergoes continuous oxidation during the TGA analysis. These observations are consistent with XRD and SEM results of the spent catalysts. To investigate the type of the deposited carbon, DTG profiles for the spent catalysts have been plotted and are shown in Fig. 11(b). There is one peak in the carbon combustion region for the spent $Ni–CoFe_2O_4$ catalysts at 615 °C. As reported, carbon deposited over $CoFe_2O_4$ had a maximum combustion rate at 630 ^{o}C [16]. It seems the presence of nickel in the $CoFe_2O_4$ catalyst may affect the deposited carbon type.
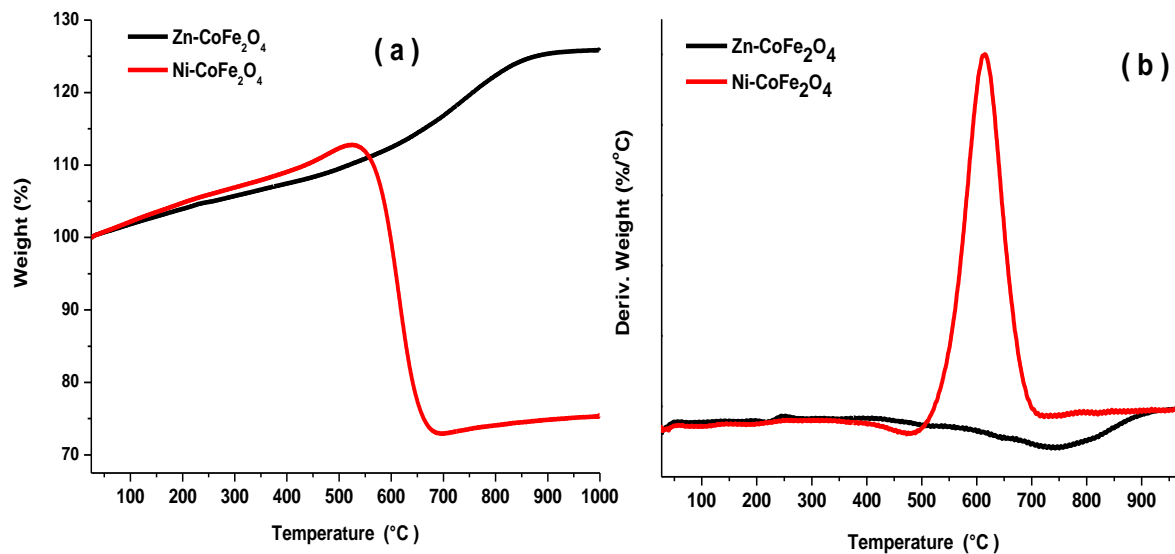
Fig. 11. (a) TGA oxidation and (b) DTG profiles for the spent $Zn-CoFe_2O_4$ and $Ni-CoFe_2O_4$ catalysts.

4. Conclusion

In this work, $Zn-CoFe_2O_4$ and $Ni-CoFe_2O_4$ were successfully synthesized using a wet chemical method. The incorporation of Ni and Zn dopants in $CoFe_2O_4$ have different effects on the $CoFe_2O_4$ characteristics as well as its catalytic performance. From the XRD results, the incorporation of Zn^{2+} and Ni^{2+} into $CoFe_2O_4$ did not alter its overall spinel based structure, yet, peak intensity/position changed. The XPS and Raman spectra indicated that Zn and Ni incorporation in $CoFe_2O_4$ led to Co^{2+} and Fe^{2+} redistribution between the tetrahedral and octahedral sites as well as increases the content of the adsorbed oxygen and oxygen vacancies in $Zn-CoFe_2O_4$ and $Ni-CoFe_2O_4$, respectively. As a result, $Ni-CoFe_2O_4$ shows better methane cracking activity in comparison to $Zn-CoFe_2O_4$ catalysts. The SEM and Raman results of the spent materials have confirmed the deposition carbon nanostructures on the surface of the spent $Ni-CoFe_2O_4$ catalyst.

Declaration of competing interest

The authors declare that they have no known competing financial interests or personal relationships that could have appeared to influence the work reported in this paper.

References

1) I.U. Din, M. Usman, S. Khan, A. Helal, M.A. Alotaibi, A.I. Alharthi, G. Centi, Prospects for a green methanol thermo-catalytic process from CO_2 by using MOFs based materials: A mini-review, Journal of CO_2 Utilization 43 (2021) 101361. https://doi.org/10.1016/j.jcou.2020.101361

2) I.U. Din, M.A. Alotaibi, A.I. Alharthi, Green synthesis of methanol over zeolite based Cu nano-catalysts, effect of Mg promoter, Sustainable Chemistry and Pharmacy 16 (2020) 100264. https://doi.org/10.1016/j.scp.2020.100264

3) I.U. Din, M.S. Shaharun, A. Naeem, M.A. Alotaibi, A.I. Alharthi, Q. Nasir, Effect of reaction conditions on the activity of novel carbon nanofiber-based Cu/ZrO_2 catalysts for CO_2 hydrogenation to methanol, Comptes Rendus. Chimie 23 (2020) 57-61. DOI: 10.5802/crchim.6

4) A.I. Alharthi, I.U. Din, M.A. Alotaibi, Effect of the Cu/Ni Ratio on the Activity of Zeolite Based Cu–Ni Bimetallic Catalysts for CO_2 Hydrogenation to Methanol, Russian Journal of Physical Chemistry A 94 (2020) 2563-2568. DOI: 10.1134/S0036024420120043

5) A.I. Alharthi, I.U. Din, M.A. Alotaibi, G. Centi, Application of cobalt ferrite nano-catalysts for methanol synthesis by CO_2 hydrogenation: Deciphering the

role of metals cations distribution, Ceramics International 47 (13) (2021) 19234-19240   https://doi.org/10.1016/j.ceramint.2021.03.149

6) U.N.E.P.U. Climate and Clean Air Coalition (CCAC) Global Methane Assessment (full report), Web Page, (2021).

7) N. Bayat, M. Rezaei, F. Meshkani, Methane dissociation to COx-free hydrogen and carbon nanofiber over Ni-Cu/Al_2O_3 catalysts, Fuel 195 (2017) 88–96. https://doi.org/10.1016/j.fuel.2017.01.039

8) D. A. Kutteri, I-Wen Wang, A. Samanta, Lili Li and J. Hu. Methane decomposition to tip and base grown carbon nanotubes and COx free H_2 over mono and bimetallic 3d transition metal catalysts, Catalysis Science &Technology.

9) S. Karimi, F. Bibak, F. Meshkani, A. Rastegarpanah, J. Deng, Y. Liu, H. Dai, Promotional roles of second metals in catalyzing methane decomposition over the Ni-based catalysts for hydrogen production: A critical review, International Journal of Hydrogen Energy, 46 (2021) 20435-20480.

10) U.P.M. Ashik , W.M.A. Wan Daud, H. F. Abbas, Production of greenhouse gas free hydrogen by thermocatalytic decomposition of methane – A review, Renewable and Sustainable Energy Reviews, 44 (2015) 221-256.

11) Anne-Claire Dupuis, The catalyst in the CCVD of carbon nanotubes- a review, Progress in Materials Science, 50 (2005) 929–961

12) C. Guéret, M. Daroux, F. Billaud, Methane pyrolysis: thermodynamics, Chemical Engineering Science 52 (1997) 815-827.
https://doi.org/10.1016/S0009-2509(96)00444-7

13) S. Ayyappan, G. Panneerselvam, M.P. Antony, J. Philip, High temperature stability of surfactant capped $CoFe_2O_4$ nanoparticles, Materials Chemistry and Physics 130 (3) (2011) 1300-1306.
https://doi.org/10.1016/j.matchemphys.2011.09.021

14) N.T. To Loan, N.T. Hien Lan, N.T. Thuy Hang, N. Quang Hai, D.T. Tu Anh, V. Thi Hau, L. Van Tan, T. Van Tran, $CoFe_2O_4$ Nanomaterials: Effect of Annealing Temperature on Characterization, Magnetic, Photocatalytic, and Photo-Fenton Properties, Processes 7(12) (2019) 885. https://doi.org/10.3390/pr7120885

15) M. Bastianello, S. Gross, M.T. Elm, Thermal stability, electrochemical and structural characterization of hydrothermally synthesized cobalt ferrite ($CoFe_2O_4$), RSC Advances 9 (2019) 33282-33289. https://doi.org/10.1039/C9RA06310B

16) Abdulrahman I. Alharthi, Mshari A. Alotaibi, Israf UdDin, E. Abdel-Fattah, Md Afroz Bakht, Ahmed Sadeq Al-Fatesh and Abdulaziz A. Alanazi. Mg and Cu incorporated $CoFe_2O_4$ catalyst: characterization and methane cracking performance for hydrogen and nano-carbon production, Ceramics International 47 (2021) 27201–27209. https://doi.org/10.1016/j.ceramint.2021.06.142

17) N.S.N. Hasnan, S.N. Timmiati, K.L. Lim, Z. Yaakob, N.H.N. Kamaruddin, L.P. Teh. Recent developments in methane decomposition over heterogeneous catalysts: an overview. *Mater Renew Sustain Energy*. 9 (8), (2020) 1-18

18) E. Meloni, M. Martino, V. Palma. A Short Review on Ni Based Catalysts and Related Engineering Issues for Methane Steam Reforming. *Catalysts, 10* (2020) 352.

19) S. K. Saraswat, B. Sinha, K. K. Pant, R. P. Gupta, Kinetic study and modeling of homogeneous thermocatalytic decomposition of methane over a Ni−Cu−Zn/Al_2O_3 catalyst for the production of hydrogen and bamboo-shaped carbon nanotubes, Ind. Eng. Chem. Res. 55 (45), (2016) 11672−11680.

20) M. Hamdan, L. Halawy, N. A. Aramouni, M. N.Ahmad, J. Zeaiter, Analytical review of the catalytic cracking of methane, Fuel. Vol 324, Part A, (2022) 124455

21) J.-H. Park, S. Yeo, T.-J. Kang, H.-R. Shina, I. Heo and T.-S. Chang, Effect of Zn promoter on catalytic activity and stability of Co/ZrO_2 catalyst for dry reforming of CH_4. Journal of CO_2 Utilization, 23 (2018) 10–19

22) Y. Jiao, J. Zhang, Y. Du, D. Sun, J. Wang, Y. Chen and Lu, J., Steam reforming of hydrocarbon fuels over M (Fe Co, Ni, Cu, Zn)-Ce bimetal catalysts supported on Al2O3. Int. J. Hydrogen Energy. 41, 10473–10482 (2015). https ://doi.org/10.1016/j.ijhydene.2015.09.151

23) X.-F. Wu, Non-Redox-Metal-Catalyzed Redox Reactions: Zinc Catalysts, Chem. Asian J. (2012). DOI: 10.1002/asia.201200596

24) I.U. Din, S. Tasleem, A. Naeem, M.S. Shaharun, Q. Nasir, Study of annealing conditions on particle size of nickel ferrite nanoparticles synthesized by wet chemical route, Synthesis and Reactivity in Inorganic, Metal-Organic, and Nano-

Metal Chemistry 46(3) (2016) 405-408. https://doi.org/10.1080/15533174.2014.988226

25) Lv. Chufei, Xu Leilei, C. Mindong, C. Yan, W. Xueying, L. Yaping, W. Caie, Y. Bo, M. Zhichao, H. Xun and S. Qinghui, Recent Progresses in Constructing the Highly Efficient Ni Based Catalysts With Advanced Low-Temperature Activity Toward CO_2 Methanation, Front. Chem. 28 (2020) 1-32. https://doi.org/10.3389/fchem.2020.00269

26) S. Lowell, J.E. Shields, M.A. Thomas, M. Thommes, M., Characterization of porous solids and powders: surface area, pore size and density. Kluwer Academic Publishers, Dordrecht (2004)

27) K. S.W. Sing and R. T. Williams, Physisorption Hysteresis Loops and the Characterization of Nano porous Materials, Adsorption Science & Technology 22 (10) 2004 773-782.   https://doi.org/10.1260/0263617053499032

28) http://abulafia.mt.ic.ac.uk/shannon/ptable.php , accessed August 22th 2022

29) M. A. Majeed Khan, W. Khan, M. Ahamed, J. Ahmed, M. A. Al-Gawati, and A. N. Alhazaa, Silver-Decorated Cobalt Ferrite Nanoparticles Anchored onto the Graphene Sheets as Electrode Materials for Electrochemical and Photocatalytic Applications, ACS Omega 5 (2020) 31076−31084 https://doi.org/10.1021/acsomega.0c04191

30) J. Hölscher, H. L. Andersen, M. Saura-Múzquiz, P.G. Garbus, M. Christensen, Correlation between microstructure, cation distribution and magnetism in Ni1-xZnxFe2O4 nanocrystallites, Cryst Eng Comm. 22 (2020) 515-524 https://doi.org/10.1039/C9CE01324E

31) C. S. S. R. Kumar, Raman Spectroscopy for Nanomaterials Characterization; Springer: Heildeberg, Germany, 2012.

32) P. Samoila, C. Cojocaru, L. Sacarescu, P.P. Dorneanu, A.A. Domocos, A. Rotaruca, Remarkable catalytic properties of rare-earth doped nickel ferrites synthesized by sol-gel auto-combustion with maleic acid as fuel for CWPO of dyes, Applied Catalysis B: Environmental, 202 (2017) 21–32. https://doi.org/10.1016/j.apcatb.2016.09.012

33) J-L Ortiz-Quinonez, U. Pal, and M. S.Villanueva. Structural, Magnetic, and Catalytic Evaluation of Spinel Co, Ni, and Co−Ni Ferrite Nanoparticles

Fabricated by Low-Temperature Solution Combustion Process, ACS Omega 3 (2018) 14986−15001 https://doi.org/10.1021/acsomega.8b02229

34) S.M. Ansari, K.C. Ghosh, R.S. Devan, D. Sen, P.U. Sastry, Y.D. Kolekar, C. Ramana, Eco-Friendly Synthesis, Crystal Chemistry, and Magnetic Properties of Manganese-Substituted $CoFe_2O_4$ Nanoparticles, ACS omega 5(31) (2020) 19315-19330. https://doi.org/10.1021/acsomega.9b02492

35) O.N. Shebanova, P. Lazor, Raman spectroscopic study of magnetite ($FeFe_2O_4$): A new assignment for the vibrational spectrum, J. Solid State Chem. 174(2) (2003) 424– 430. https://doi.org/10.1016/S0022-4596(03)00294-9

36) R. Topkaya, A. Baykal and A. Demir, Yafet–Kittel-type magnetic order in Zn-substituted cobalt ferrite nanoparticles with uniaxial anisotropy, J. Nanopart. Res. 15 (2013) 1359. https://doi.org/10.1007/s11051-012-1359-6

37) D. Varshney, K.Verma, A. Kumar, Substitutional effect on structural and magnetic properties of $A_x Co_{1-x} Fe_2O_4$ (A=Zn, Mg and x=0.0, 0.5) ferrites, J. Mol. Struct. 1006(1-3) (2011) 447–452. https://doi.org/10.1016/j.molstruc.2011.09.047

38) J. Chastain, R.C. King Jr, Handbook of X-ray photoelectron spectroscopy, Perkin-Elmer Corporation, (1992) 40, 221.

39) M. Zhang, X. Yang, X. Kan, X. Wang, L. Ma, M. Jia, Carbon-encapsulated $CoFe_2O_4$/graphene nanocomposite as high performance anode for lithium ion batteries, Electrochimica Acta 112 (2013) 727-734. DOI: 10.1016/j.electacta.2013.09.034

40) Y. Wang, Y. Zhang, S. Zhao, J. Zhu, L. Jin, H. Hu, Preparation of bimetallic catalysts Ni-Co and Ni-Fe supported on activated carbon for methane decomposition, Carbon Resources Conversion 3 (2020) 190-197. DOI: 10.1016/j.crcon.2020.12.002

41) D. Torres, J. L. Pinilla and I. Suelves, Co-, Cu- and Fe-Doped Ni/Al_2O_3 Catalysts for the Catalytic Decomposition of Methane into Hydrogen and Carbon Nanofibers, Catalysts, 8(8) (2018) 300. https://doi.org/10.3390/catal8080300

42) A. Gamal, Kamel Eid, M. H. El-Naas, D. Kumar and A. Kumar, Catalytic Methane Decomposition to Carbon Nanostructures and COx-Free Hydrogen: A Mini-Review, nanomaterials 11(5) (2021) 1226. https://doi.org/10.3390/nano11051226

43) G. Urdiana, R. Valdez, G. Lastra, M.Á. Valenzuela and A. Olivas, Production of hydrogen and carbon nanomaterials using transition metal catalysts through methane decomposition, Materials Letters 217 (2018) 9–12. https://doi.org/10.1016/j.matlet.2018.01.033

44) H. Ogihara, N. Imai and H. Kurokawa, Decomposition and coupling of methane over Pd-Au/Al_2O_3 catalysts to form COx-free hydrogen and C_2 hydrocarbons, International Journal of Hydrogen Energy 45(58) (2020) 33612-33622. https://doi.org/10.1016/j.ijhydene.2020.09.136

45) R. Aiello, J. E. Fiscus, H-C zur Loye, M. D. Amiridis, Hydrogen production via the direct cracking of methane over Ni/SiO_2: catalyst deactivation and regeneration, Applied Catalysis A: General 192(2) (2000) 227–234. https://doi.org/10.1016/S0926-860X(99)00345-2

46) M.A. Pimenta, G. Dresselhaus, M.S. Dresselhaus, L.G. Cancado, A. Jorio and R. Saito, Studying disorder in graphite-based systems by Raman spectroscopy, Physical Chemistry Chemical Physics, 9 (2007) 1276-1290. https://doi.org/10.1039/B613962K